Biogeosciences
Discussions

Biological response to hydrodynamic factors in estuarine-coastal systems: a numerical analysis in a micro-tidal bay.

Marta F-Pedrera Balsells [1]*, Manel Grifoll[1], Margarita Fernández-Tejedor[2], Manuel Espino[1], Marc Mestres[1], Agustín Sánchez-Arcilla[1].

[1] Maritime Engineering Laboratory (LIM), Catalonia University of Technology (UPC), 08034 Barcelona, Spain;

[2] Institute of Agriculture and Food Research and Technology (IRTA), Crtra. Poble Nou, s/n Km 5,5. 43540 Sant Carles de la Rapita, Spain;

* Correspondence: marta.balsells@upc.edu (M.F-P.B.)

Abstract:

Phytoplankton primary production in coastal bays and estuaries is influenced by multiple physical variables, such as wind, tides, freshwater inputs or light availability. In a short-term perspective these factors may influence the composition of biological variables such as phytoplankton biomass, as well as the amount of nutrients within the waterbody. Observations in Fangar Bay, a small, shallow, stratified and micro-tidal bay in the Ebro Delta (NW Mediterranean Sea), have shown that during wind episodes the biological variables undergo sudden variations in terms of concentration and distribution within the bay. The Regional Ocean Model System (ROMS) coupled with a nitrogen-based nutrient, phytoplankton, zooplankton, and detritus (NPZD) model has been applied to understand this spatio-temporal variability of phytoplankton biomass in Fangar Bay. Idealised simulations prove that during weak wind events (< 6 m·s^{-1}), the stratification is maintained and therefore there is not dynamic connection between surface and bottom layers, penalizing phytoplankton growth in the whole water column. Conversely, during intense wind events (> 10 m·s^{-1}) water column mixing occurs, homogenising the concentration of nutrients throughout the column, and increasing phytoplankton biomass in the bottom layers. In addition, shifts in the wind direction generate different phytoplankton biomass distributions within the bay, in accordance with the dispersion of freshwater plumes from existing irrigation canals. Thus, the numerical results prove the influence of the freshwater plume evolution on the phytoplankton biomass distribution, which is consistent with remote sensing observations. The complexity of the wind-driven circulation due to the bathymetric characteristics and the modulation of the stratification implies that the phytoplankton biomass differs depending on the prevailing wind direction, leading to sharp Chl *a* gradients and complex patterns.

Keywords: phytoplankton biomass, ROMS-NPZD model, wind, biological parameters, physical parameters, Fangar Bay.

1. Introduction

The intense biological activity of estuaries and coastal bays and their importance as a source of resources and socio-economic services is well known. The use of these areas as aquaculture zones has provided great benefits as well as great problems (Ramón et al., 2007; Llebot et al., 2010, 2011; Soriano-González et al., 2019). The influence of the terrestrial environment and human activity in these domains provide the nutrients necessary to create ecosystemic value (Lohrenz et al., 1997). The biological evolution of these waterbodies is strongly affected by physical factors. For instance, strong winds may controls the inner water circulation (Geyer, 1997; Alekseenko et al., 2013; Cerralbo et al., 2015) and, together with topographic effects, can even cause the current to flow against the wind direction in the central channels (Xie & Li, 2018; F-Pedrera Balsells et al., 2020a). Freshwater inputs can also have a considerable effect on the water circulation (Cerralbo et al., 2014) and, acting as fluvial nutrient suppliers, can determine the temporal and spatial variability of phytoplankton biomass (Geyer et al., 2018; Jiang et al., 2020). In this sense, the use of coupled physico-biological numerical models as a tool to understand the complexity of the phytoplankton regulatory mechanism in estuaries has increased in recent years, complementing *in situ* data and satellite imagery (Llebot et al., 2010; Artigas et al., 2014; Jiang et al., 2020). These numerical models can provide information on the current state of the estuary, create hypotheses and numerical experimentation, and predict certain events and ecosystem responses (Stow et al., 2009; Llebot et al., 2010).

51 In small and shallow estuaries, the effects of both the physical and biological mechanisms become more
52 complex due to the geometry of the basin itself. Moreover, in the bays of the Ebro Delta (i.e. Alfacs in the
53 southern hemidelta and Fangar in the northern hemidelta), freshwater discharges from rice field irrigation
54 channels also play an important role, together with aquifer contributions, being an important source of
55 nutrients for the coastal areas (Jou et al., 2019), both inorganic and organic. In a small-scale coastal bay
56 such as Fangar Bay, where depths are only of a few metres, chlorophyll a (Chl a) concentrations tend to
57 show a high variability on a seasonal scale rather than on an interannual scale (Llebot et al. 2011), with
58 higher concentrations found during the summer (Ramón, Fernández, and Galimany 2007). In this sense,
59 Chl a concentrations in Fangar Bay tend to show a larger variability as compared to other coastal domains
60 such as the Ría de Arousa (Ramón, Fernández, and Galimany 2007) or Alfacs Bay (Artigas et al. 2014).
61
62 Previous investigations in Fangar Bay revealed that, during wind episodes, the biological variables
63 undergo sudden variations in terms of concentration and distribution within the bay (F-Pedrera Balsells et
64 al., 2021). *In situ* measurements obtained during specific field campaigns and remote sensing observations
65 suggested a link between the breaking of the stratification during these episodes and the Chl a distribution
66 in the bay, with intense winds causing an increase in the Chl a concentration values. The role of the
67 discharges from the irrigation canals remained unclear because the freshwater outflow was constant during
68 the field campaigns. However, the spatial-temporal variability of the Chl a concentration observed in the
69 field campaigns was quite complex due to the many factors involved, and deserved additional modelling
70 efforts. The purpose of the present study is to further this first assessment by investigating the biological
71 response of the bay to wind episodes and freshwater inputs through the combination of idealised numerical
72 simulations and observations. For this, a biological model is embedded into a validated hydrodynamic
73 model to reproduce the dynamics within the bay. Extensive field data and previous hydrodynamic
74 knowledge converts Fangar Bay in a unique study area to investigate the biological response in an area with
75 large spatio-temporal variability on Chl a evolution.
76
77 The paper is organised as follows: Section 2 presents a detailed description of the study area and the
78 model used, as well as a brief description of the pre-processing satellite images. Section 3 presents the
79 results of the numerical simulations concerning the evolution phytoplankton, salinity and nutrients, as well
80 as a comparison with satellite images. Section 4 discusses the effects of the wind and freshwater plume on
81 the biological variables comparing with sites. Finally, section 5 summarises the main conclusions and
82 suggests future works to be carried out.
83
84 **2. Material and Methods**

85 2.1. Study area
86
87 Fangar Bay is part of the Ebro Delta (NW Mediterranean Sea), which reaches about 25 kilometres
88 offshore and forms two semi-enclosed bays, Fangar to the north and Alfacs to the south. Of these, Fangar
89 Bay is the smallest, extending over 12 km^2, with a length of about 6 km, a maximum width of 2 km and a
90 volume of water of 16x10^6 m^3 (Delgado and Camp 1987). The average depth is 2 m, with a maximum of 4
91 m (see bathymetry in Figure 1). Its connection with the open sea is oriented to the NW, and is approximately
92 1 km wide (Garcia and Ballester 1984), although it is currently narrowing because of the accumulation of
93 sediment from the beach located to the north (Archetti, Bernia, and Salvà-Catarineu 2010).
94
95 The wind regime in the Fangar Bay area is characterized by the presence of S/SE sea breezes – which
96 do not exceed 6 m·s^{-1} during spring and summer– and strong winds from the N and NW of more than 12
97 m·s^{-1} in autumn and winter (Bolaños et al. 2009; Grifoll et al. 2016). The most frequent wind throughout
98 the year is locally known as Mistral, which is characterized by strong gusts of cold and dry wind from the
99 NW (Garcia and Ballester 1984). These winds are associated to the general weather pattern and occur
100 throughout the year, but show maximal strength and persistence during the colder months. Additionally, E
101 and NE winds that can also be quite intense (~10 m·s^{-1}) are responsible for local rain events and transient
102 increases of the local mean sea level at the coast (Muñoz 1990).
103

104   Both the Ebro Delta bays receive freshwater inputs from the canals irrigating the Delta paddies. This
105   freshwater outflow is regulated by the rice cultivation cycle throughout the year. In Fangar Bay, the canals
106   are open between April and November, discharging a mean flow of 7.23 $m^3 \cdot s^{-1}$ (*SAICA Project, 2013.*
107   *Available online: https://www.saica.co.za/ (accessed on 30 January 2020)*), whereas the outflow is
108   negligible from December to March, when the channels are closed (Perez & Camp, 1986). There are two
109   main freshwater discharges in Fangar Bay: one in the Illa de Mar harbour inside the bay (IM in Figure 1)
110   and the other one, Bassa de les Olles, located at the bay mouth (BO in Figure 1). In addition to these,
111   freshwater inputs are also expected inside the bay from groundwater sources (Camp and Delgado 1987),
112   and along the coastline where freshwater inflows regulated by gravity according to the sea level occur. In
113   both cases, the expected freshwater inflow is smaller than that discharged from the regulated irrigation
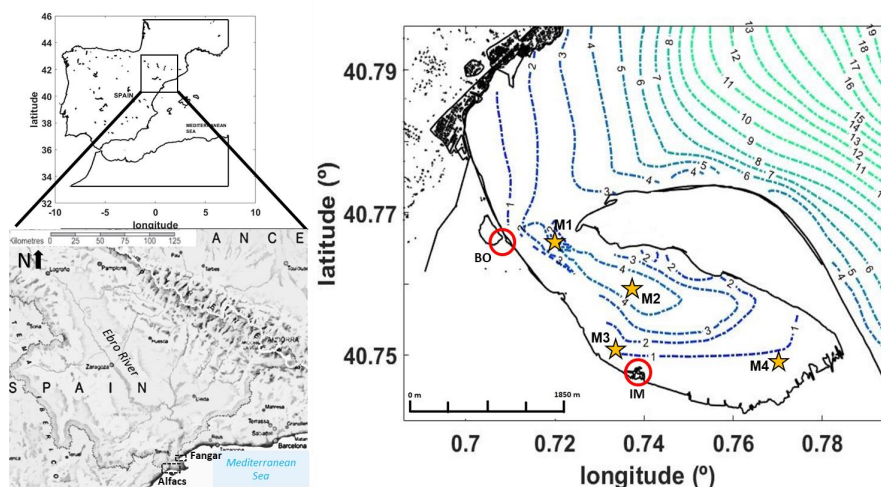114   channels.

115
116

Figure 1. Location of the study area. The red circles show the two main points of freshwater discharges (Bassa de les Olles (BO) and Illa de Mar (IM). The yellow stars show the location of the control points used for the numerical model results. The bathymetry is also shown in the figure.

117

118   Fangar Bay is micro tidal, with a tidal range smaller than 1 m, which accentuates the action of the wind,
119   and is stratified most of the year mainly due to the freshwater flows rather than to the atmospheric heat
120   fluxes. Because of its bathymetry and complex geometry there is a strong transverse variability of the water
121   flows, particularly for prevalent up-bay wind episodes (NW winds), during which up-bay flow occurs in
122   the lateral shoals and down-bay flow in the central channel for up-bay wind pulses. These winds also cause
123   homogenisation of the whole water column. On the other hand, during calm periods the water circulation
124   is complex: current velocities are very small and lack a clear pattern, and the bay is strongly stratified due
125   to the freshwater inputs from the drainage channels (F-Pedrera Balsells et al., 2020a).

126
127   2.2. Numerical model and experiments design

128   A set of numerical experiments were conducted using the Regional Ocean Model System (ROMS) to
129   analyse the link between the hydrodynamic and Chl *a* response to the wind in small and shallow estuaries.
130   The ROMS numerical model is a 3D, free-surface, terrain-following numerical model that solves the
131   Reynolds-Averaged Navier-Stokes equations using hydrostatic and Boussinesq assumptions (Shchepetkin
132   and McWilliams 2005). ROMS uses the Arakawa-C differentiation scheme to discretize the horizontal grid
133   in curvilinear orthogonal coordinates and finite difference approximations on vertical stretched coordinates
134   (Haidvogel et al. 2007). The numerical details of ROMS are described extensively in (Shchepetkin and
135   McWilliams 2005). This model has been used and validated in similar bays and estuaries, such as Alfacs

Biogeosciences
Discussions

Open Access

EGU

136 Bay located south of the Ebro Delta (e.g. (Cerralbo et al., 2014, 2015, 2019)) and in the Fangar Bay (see
137 Annex 1). The domain used for the experiments consists of a regular 107x147 grid with a horizontal
138 resolution of about 70 m and 10 sigma levels in the vertical direction. The model boundary is located 10
139 points away of the mouth entrance to avoid boundary noise. The hydrodynamic bottom boundary layer was
140 parametrised with a logarithmic profile using a characteristic bottom roughness height of 0.2 m. The
141 turbulence closure scheme for the vertical mixing was the generic length scale (GLS) tuned to behave as a
142 k-ε (Warner et al., 2005). Horizontal harmonic mixing of momentum was defined with constant values of
143 $5 \ m^2 \cdot s^{-1}$.

144
145 The NPZD numerical model coupled with ROMS model includes dissolved inorganic nitrogen,
146 phytoplankton, zooplankton and detritus (Franks 2002). The initial nitrate concentration was taken from
147 field data collected by IRTA between the years 2009-2012 (ACA, 2012), and the initial phytoplankton
148 concentrations were collected from observation data during the year 2019, whereas the initial zooplankton
149 concentration was estimated from the literature (Rico 2015; Powell et al. 2006). The units in which these
150 data were collected were $mg \cdot m^{-3}$. The NPZD model uses $mmol \cdot m^{-3}$ units, so a conversion has been made
151 using the mole fraction of Chl a (see Table 1). The rest of input variables for the ROMS-NPZD model were
152 acquired from Llebot et al. (2010), and are detailed in Appendix B (Table B1), together with the model
153 equations. Short-term simulations (5 days each) were carried out to analyse the response of biological
154 variables to the wind. This simulation length exemplifies the typical wind events in the area, lasting from
155 3 to 5 days (except the daily sea breeze during spring and summer). Six experiments were designed, varying
156 the wind direction and intensity, as well as the freshwater from the channels. The wind parameters are based
157 on wind measurements in the Fangar area (F-Pedrera Balsells et al., 2020a), with weaker down-bay winds
158 (associated to daily sea breeze, DW6 simulation), NW up-bay winds (UW10 simulation), strong NW up-
159 bay winds (UW12 simulation) and SE down-bay winds (DW8 simulation). For theoretical comparison, a
160 simulation was also carried out with 0 $m \cdot s^{-1}$ wind intensity (CALM simulation). All simulations are
161 summarized in Table 1. Temperature and salinity conditions were in accordance with those measured within
162 the bay (see field campaign description in F-Pedrera Balsells et al., 2021). Freshwater inputs were activated
163 to monitorize the evolution of nutrient inputs from the irrigation channels. Both channels (BO and IM,
164 Figure 1) provides nutrients that will be presumably dispersed within the bay due to the combined action
165 of currents and wind.

166 **Table 1. Summary of the idealized numerical simulations using the ROMS-NPZD model for Fangar Bay.**

Simulation	Wind direction	Intensity wind ($m \cdot s^{-1}$)	Channel flow ($m^3 \cdot s^{-1}$ each channel)	Initial nitrate concentration ($mmol \cdot m^{-3}$)	Initial phytoplankton biomass ($mmol \cdot m^{-3}$)	Initial zooplankton biomass ($mmol \cdot m^{-3}$)
CALM	-	0	7.5	2.73	0.27	0.08
DW6	Down-bay wind	6	7.5	2.73	0.27	0.08
UW10	Up-bay wind	10	7.5	2.73	0.27	0.08
DW8	Down-bay wind	8	7.5	2.73	0.27	0.08
UW12	Up-bay wind	12	7.5	2.73	0.27	0.08
UW12fr	Up-bay wind	12	3	2.73	0.27	0.08

167
168

169   2.3. Satellite image processing
170

171   To qualitatively compare the numerical modelling results with real observations, satellite images from
172 Sentinel-2, level 1-C, are used. These satellites carry a single optical instrument, the MultiSpectral Imager
173 (MSI), and its swath width (290 km) and high revisit time (10 days at the equator with one satellite and 2–
174 3 days at mid-latitudes) support monitoring of Earth's surface changes. Chlorophyll a concentrations were
175 computed   automatically   by   the   Sentinel   Application   Platform   (SNAP)
176 (https://step.esa.int/main/toolboxes/snap/, accessed on 25 February 2021). The MSI sensor has had an
177 atmospheric correction applied to it with a C2RCC processor (Case 2 Regional CoastColour, Brockmann
178 et al., 2016) to obtain the Chl a images. The images correspond to remote sensing obtained after intense
179 wind episodes (see details in F-Pedrera Balsells et al., 2021).

180
181 **3. Results**

182   Four points within the bay have been chosen to investigate the temporal evolution of the biological
183 variables obtained from the NPZD model: in the mouth area (M1), in the centre of the bay (M2), in a coastal
184 area in front of the IM discharge point (M3) and in the innermost part of the bay (M4). Both channels (BO
185 and IM, Figure 1) provide nutrients which increase the concentration of phytoplankton biomass within the
186 bay. Figure 2 shows the time series of the numerical simulation in terms of nitrates and phytoplankton at
187 the four control points. The nitrate concentration tends to decrease gently during the simulation, consistently
188 with the increase in phytoplankton biomass and zooplankton. All simulations show larger concentrations
189 of phytoplankton biomass at the surface due to the freshwater fluxes, as will be discussed later. Substantial
190 differences of phytoplankton biomass between surface and bottom layers are evident in M1, where the
191 stratification tends to be larger in contrast to the shallowest point (M4). The inner point M4 also shows a
192 clear correlation of the wind intensity and the phytoplankton biomass values: as the up-bay wind intensity
193 increases (i.e. UW12, larger than UW10) the phytoplankton biomass also increases. In all cases the
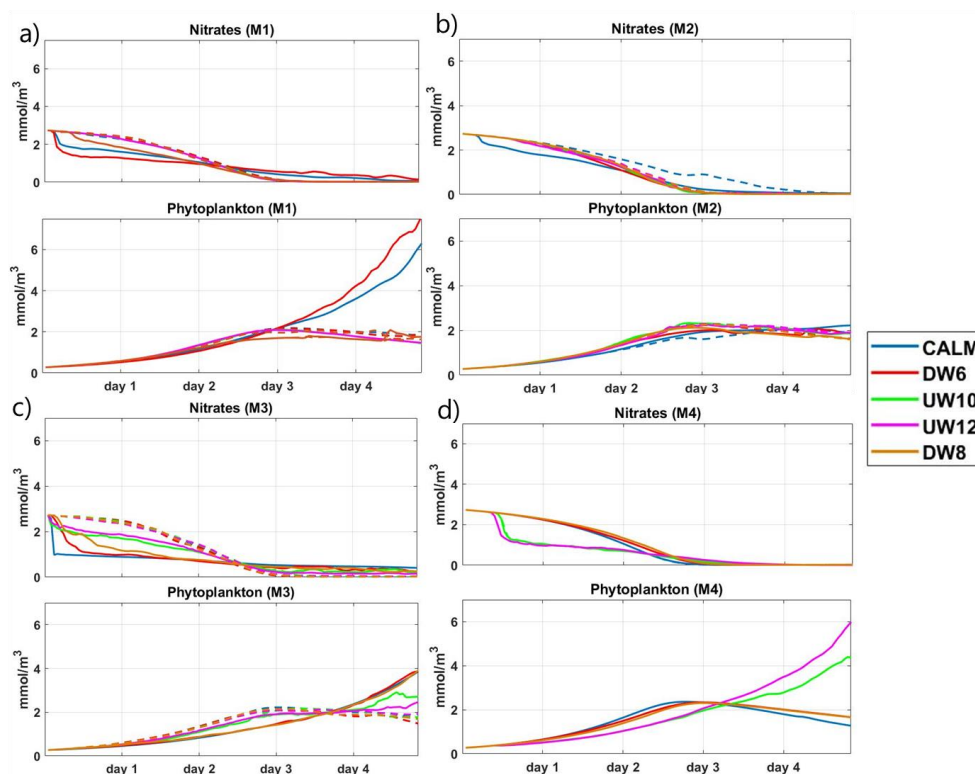194 numerical simulations suggest large temporal and spatial variability within the bay.

Figure 2. Time series of the nitrates and phytoplankton biomass at different points of the bay: (a) M1, (b) M2, (c) M3 and (d) M4. The different colours show the different simulations with in function of the wind. Solid line shows surface numerical results, dashed line shows bottom numerical results.

Intense wind was associated to the homogenisation of the initially stratified water column for strong wind episodes. In particular, for the UW10 and UW12 simulations (moderate and strong up-bay wind), both surface and bottom phytoplankton time series coincide at all control points. Figure 3 shows the vertical profiles of phytoplankton biomass and salinity after three days simulation at the four points mentioned above for the DW6 (weak down-bay wind), DW8 (SE down-bay wind) and UW12 (NW up-bay wind) simulations. These profiles show homogeneous concentrations of phytoplankton biomass and salinity in the water column after strong wind episodes (DW8 and UW12). In contrast, during weaker winds (DW6) the saline stratification tends to remain in M1 and M3, leading to larger presence of phytoplankton biomass in the surface layers. At the innermost point of the bay (i.e., M4), the phytoplankton biomass is homogeneous in all simulations since, due to the shallowness of the area (lesser than 1 m deep), even weaker winds are able to mix the water column. The comparison of profiles at M3 shows a high variability of phytoplankton biomass values: DW8 shows larger values of phytoplankton biomass as compared to DW6. This means that the mixing mechanism can favour the increase of phytoplankton biomass. Finally, the comparison in M3 between DW8 and UW12 also suggests the effect of the freshwater plume on the phytoplankton biomass, which will be discussed later.

Differences in growth rates between phytoplankton and zooplankton biomass are observed in the time series. While phytoplankton can multiply rapidly under favourable concentrations of light and nutrients, increases in zooplankton numbers often lag considerably behind due to their slower generation times. Consequently, when phytoplankton biomass peaks and nutrients decline, zooplankton biomass may remain low as they begin to grow in response to the high food supply (Figure not shown). These relations are consistent with the diagram shown in the Appendix B (B1).
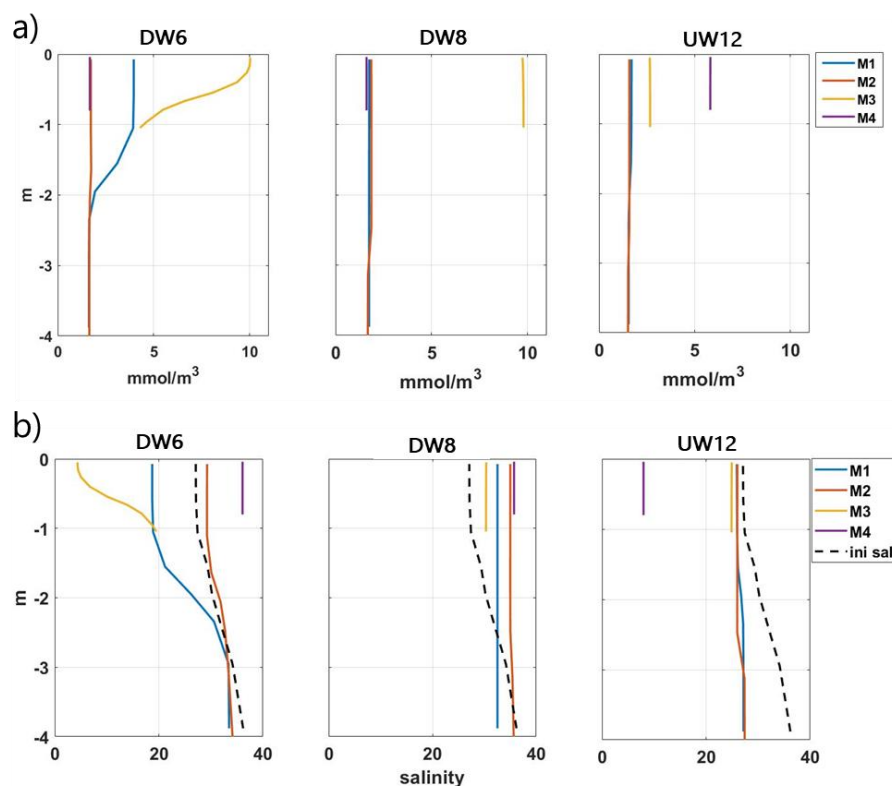
Figure 3. Vertical Chl *a* profiles (a) and vertical salinity profiles (b) as a function of wind events simulations at the four sampling points: M1 (blue), M2 (orange), M3 (yellow) and M4 (purple). Dashed black line shows the initial salinity.

Differences in the horizontal distribution of phytoplankton biomass are also observed in Figure 3a. During calm winds, the highest biomass value is found in front of the freshwater discharge points (M1 and M3). During strong NW up-bay winds (UW12), the highest biomass values are found in the innermost area of the bay (M4), while during strong SE down-bay winds (DW8) the largest biomass concentration is observed at the coastal point inside the bay (i.e., M3), with higher values than during the DW12 simulation.

In order to examine the spatial variability, Figure 4a shows the differences in phytoplankton biomass at the end of the simulation in comparison to the initial concentration values. Surface and bottom values are displayed according to the terrain following sigma coordinates of the numerical model. All the simulations present positive values, indicating an increase of phytoplankton biomass due to the nutrients provided by the freshwater. During up-bay winds (simulations UW12 and UW12fr), the phytoplankton biomass increases in the inner zone, both at the surface and at the bottom, with concentrations larger than 5 mmol·m^{-3}. This coincides with vertical mixing of the water column, as shown by the salinity distributions (Figure 4b). In contrast, during no wind and weak (DW6) winds, the highest phytoplankton biomass (4 mmol·m^{-3}) is located in front of the discharge points, with the largest values obtained at the point inside the bay (M3, 10 mmol·m^{-3} at the surface). For no wind simulation (CALM simulation) stratified conditions remain. In this case, bottom concentrations are small (1 mmol·m^{-3}) in comparison to other cases, highlighting the positive effect of strong winds on the vertical distribution of phytoplankton biomass. During the DW8 simulation, the highest concentrations are also observed near the discharge points (M1 and M3), with the highest values found towards the mouth, consistent with the presence of a low-salinity plume. Overall, there is a correspondence between the freshwater plume and the phytoplankton biomass. Therefore, the wind-driven evolution of the plume has a very important impact on the final distribution of

241   Chl *a*. In the same way, it can be seen in Figure 3 that winds of similar intensities but different directions
242   (DW8 vs. UW10) lead to very different results in terms of the horizontal distribution of phytoplankton
243   biomass. Finally, the results of an additional simulation similar to UW12 but with half the canals' outflow
244   rates (UW12fr) revealed a horizontal distribution similar to UW12, but with smaller phytoplankton biomass
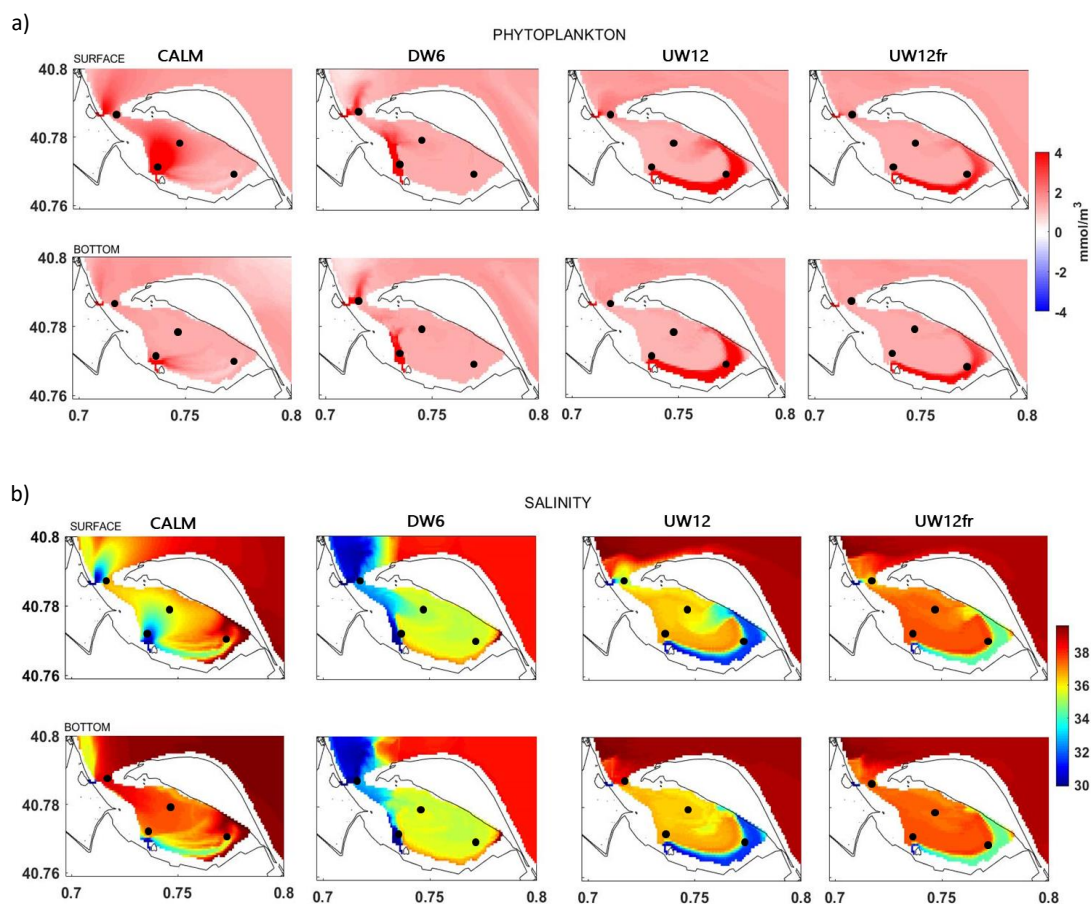245   concentrations associated to a lower nutrient input.

Figure 4. Differences in phytoplankton biomass (surface and bottom) at the end of the simulation in comparison to the to the initial concentration values (a) and surface and bottom salinity (b) according to different numerical simulations. The numerical control points are also marked with black dots.

246   Figure 5 shows a comparison between the model results and the Sentinel-2 satellite images, in periods
247   of calm or weak wind, and strong wind which produces mixing (NW up-bay wind). The satellite images
248   correspond to 15-Jul-2019 (Figure 5d) and 11-Aug-2019 (Figure 5c), one day after an up-bay wind episode
249   occurred on 14-Jul-2019, and during a sea-breeze period (weak winds) between 30 July and 12 August,
250   respectively. Note that the satellite image of the up-bay wind episode is from a few days after the wind has
251   blown, while the model results correspond to the blowing of a steady wind. In spite of this, there is an
252   identifiable correlation between model and images. For calm or weak down-bay wind (sea breeze), the
253   phytoplankton biomass is relatively low, only present in the areas close to the discharge channels following
254   the coastline consistent with the wind-driven currents due to sea breeze. During NW up-bay winds,
255   phytoplankton biomass increases in the inner zone and is later dispersed within the bay. In any case, it
256   should also be taken into account that the satellite, being such a shallow area, does not only show data on

257 phytoplankton chlorophyll but also on macrophytes, which are very present in this bay (Soriano-González
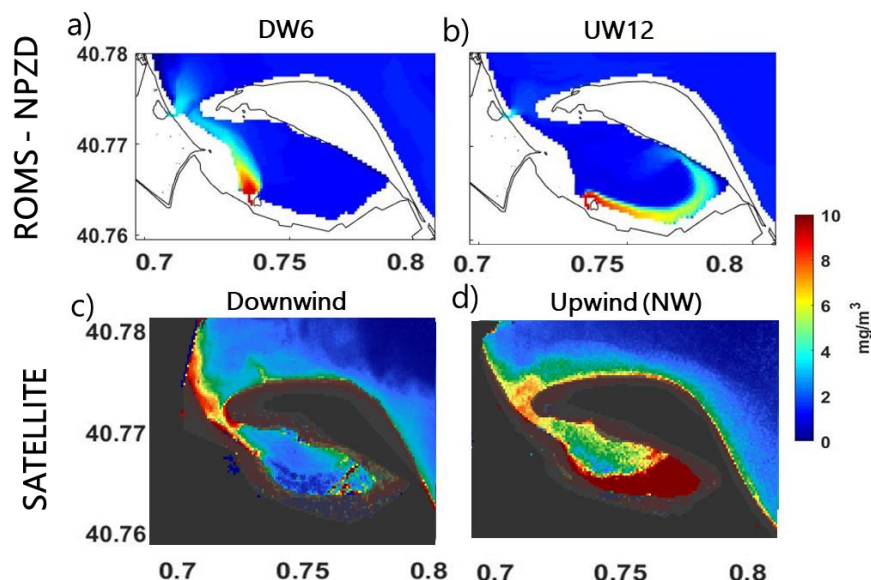258 et al. 2019).

Figure 5. Comparison of surface model results with Sentinel 2 satellite images. (a) and (b) show model results during breezes and strong NW winds, respectively. (c) and (d) show corresponding satellite images with the same wind episodes.

259
260
261 **4. Discussion**
262
263   The phytoplankton distribution is controlled by turbulent mixing and advection factors, which are
264 affected by physical forcings such as wind, tides and continental freshwater input. In tidally dominated
265 estuaries or upwelling areas, phytoplankton biomass is distributed according to spring blooms, where algal
266 blooms generated during upwelling events are transported to the bays through various physical mechanisms
267 (tidal stirring, and gravitational and wind-driven circulation (Hickey and Banas, 2003; Martin et al., 2007),
268 as occurs in the Eastern Scheldt Bay (Jiang et al. 2020) or the Rías Baixas of Galicia (Reguera et al., 1993).
269 On the other hand, in estuaries where the tide is practically non-existent and the depth is small,
270 phytoplankton growth is limited by nutrients and the turbidity of the water due to large inputs of sediment
271 from rivers and channels, such as in the Chilika lagoon (Srichandan et al., 2015) or our study area, the
272 Fangar Bay.
273
274   From a hydrodynamic point of view Fangar Bay is complex due to its shallowness and intricate
275 bathymetry (Llebot, 2010; F-Pedrera Balsells et al., 2020a). Llebot et al. (2010) implemented a numerical
276 model in Fangar Bay to determine the temporal distribution of phytoplankton and nutrients throughout the
277 year. They determined that the highest concentration of phytoplankton occurred during the first months of
278 the year with open irrigation channels, i.e., in the spring and early summer, but the role of episodic wind
279 events remained unclear. The present study is centred on the phytoplankton distribution resulting from
280 different short-term wind episodes typical of the Ebro Delta area, and focuses on the summer months for
281 which the bio-hydrodynamics are well defined (F-Pedrera Balsells et al., 2021). The numerical results have
282 proved that the wind affects the direction and magnitude of surface currents, disperses or reinforces fronts,
283 and induces vertical mixing, in accordance with other investigations (Geyer, 1997; Llebot et al., 2014; F-
284 Pedrera Balsells et al., 2020a). The distribution of phytoplankton biomass in Fangar Bay agrees with water

285 currents driven by the local winds and modulated by the complex bathymetry of the basin (F-Pedrera
286 Balsells et al., 2020a) and the evolution of the freshwater plume of the drainage channels (Figure 4b).

288   The model results have shown the combined effect of the wind on phytoplankton biomass distribution
289 within the bay from two perspectives. On the one hand, intense wind episodes are able to break the
290 stratification, mixing the water column and leading to an increase of phytoplankton biomass in the deeper
291 levels of the bay. Simulations with no wind (CALM), in which the bay remains stratified, are characterized
292 by the presence of a physical barrier that prevents nutrient vertical transfer, so the phytoplankton biomass
293 remains in the surface layers. This case shows how the absence of wind (or even the presence of sea breezes)
294 causes the phytoplankton biomass dispersion to be governed by the estuarine circulation of the bay, with
295 phytoplankton biomass decreasing in the seaward direction. A similar seaward negative gradient of
296 phytoplankton is found in other estuaries and coastal systems in which the nutrient gradients control the
297 phytoplankton distribution (Soetaert et al., 2006; Gomez et al., 2018). When strong NW up-bay winds blow
298 in Fangar Bay, the water column homogenises, making nutrients available throughout the column, both at
299 the surface and at the bottom (i.e., UPW10 and UW12 simulations). The phytoplankton biomass is advected
300 towards the inner part of the bay, following the water currents induced by the NW winds, not only at the
301 surface but throughout the water column. With strong SE down-bay winds (DW8 simulation),
302 phytoplankton biomass increases near the discharge channels and the phytoplankton biomass distribution
303 follows the water circulation driven by SE winds: seaward flow in the lateral shoals (F-Pedrera Balsells et
304 al., 2020a). The strong winds episodes suggest a non-uniformly distribution of phytoplankton biomass with
305 irregular patterns and patches attributed to a dominant source factor (see examples in Ahel et al., 1996;
306 Geyer et al., 2018; Jiang et al., 2020), which in the case of Fangar Bay is a role played by the discharge
307 channels. In consequence, following the categorization exposed by Jiang et al. (2020) in terms of spatial
308 patterns of phytoplankton biomass in estuaries and coastal bays, Fangar Bay may be included in different
309 typologies depending on the wind configuration from a short-term perspective.

311   The second effect of the wind is related to the wind-driven plume dispersion. Freshwater discharges
312 from the irrigation channels are the dominant driver of salinity and nutrient gradients. In Fangar Bay there
313 is a colimitation of nitrogen and phosphorus, with the most limiting nutrient changing throughout the year,
314 depending on the variability of sources and sinks of both nutrients (Llebot et al. 2010). The NPZD model
315 considers nitrogen only and assumes no phosphorus limitation in phytoplankton growth. This sets a limit
316 on the full understanding of Fangar Bay's dynamics, but our analysis provides a first interpretation of the
317 data. Freshwater discharges also vary over the year, depending on whether these irrigation channels are
318 closed (January to March), open (April to November) or semi-open (November and December). In F-
319 Pedrera Balsells et al. (2021) it was observed that after strong NW up-bay wind episodes in the bay,
320 phytoplankton biomass tends to increase within the bay, but it could not be determined whether this
321 behaviour extended to the entire water column as the simulations presented herein suggest. As described in
322 other works (Simpson & Bowers, 1981; Horsburgh et al., 2000) vertical density stratification is an important
323 determinant of ecosystem characteristics.

325   Ultimately, as a small, shallow, micro-tidal bay, wind generates very complex currents and causes large
326 spatial and temporal variability in the distribution of phytoplankton biomass. Chl *a* peaks usually form at
327 the front of the river plume, either by rapid nutrient assimilation and growth or by aggregation along the
328 strong salinity gradient of this transition (Geyer et al., 2018). This explains why the highest biomass levels
329 can be found following the river plume, as shown in Figure 4. Therefore, the same simulations were
330 performed by halving the channel outflow and the results on phytoplankton biomass distribution were the
331 same, only lower, due to lower nutrient input. Some studies have shown that Chl *a* concentration is higher
332 in the freshwater areas of the bay and decreases as salinity increases. This leads to high phytoplankton
333 biomass in the plume formed by freshwater tributaries, which discharge high levels of nutrients, as can
334 happen in the Scheldt River and Western Scheldt Estuary in Belgium (Soetaert et al., 2006).

336   Freshwater discharges from irrigation channels also control water residence times within the bay.
337 Prolonged residence times generally facilitate the growth and accumulation of phytoplankton biomass (Wan
338 et al. 2013). The location and magnitude of phytoplankton biomass can be partly explained by residence
339 time, although phytoplankton productivity may be affected by other factors such as nutrient availability,
340 light, temperature and zooplankton grazing (Wan et al. 2013). In Fangar Bay, residence time is in the range

Biogeosciences
Discussions

Open Access

341 of about 20 days in the middle zone and about 40 days in the innermost quasi-stagnant zone (F-Pedrera
342 Balsells et al., 2020b). This work also shows that an increase in freshwater discharge through the inner
343 channel (IM) helps to decrease the residence time in the innermost zone (F-Pedrera Balsells et al., 2020b).
344 In turn, therefore, a reduction in river discharge increases residence time and may allow a higher
345 concentration of phytoplankton to accumulate within the estuary. Our results show a higher concentration
346 of phytoplankton biomass in the innermost zone consistent with the larger residence time.
347
348 **5. Conclusions and future works**
349
350   Results based on *in situ* and remote observations and numerical models conclude that the biological
351 variables in small-scale, shallow and micro-tidal bays (such as Fangar Bay) shows strong gradients due to
352 the influence of the wind and the freshwater plume evolution. Strong winds have a double impact: i)
353 breaking down the stratification and mixing the water column, leading to an increase of phytoplankton
354 biomass at the bottom, and ii) distributing the canal-borne nutrients within the bay, resulting in an irregular
355 pattern of phytoplankton biomass. Due to the predominance of the wind forcing on the bay's water
356 circulation, different wind directions and/or intensities may have a completely different effect on
357 phytoplankton biomass distribution. In this sense, wind variability explains the complex pattern of
358 phytoplankton biomass observed in the *in situ* measurements and remote sensing, characterized by sharp
359 horizontal gradients. In particular, the link between the hydrodynamics and the phytoplankton evolution in
360 Fangar Bay can be summarized as shown in Figure 6. This figure is a conceptual diagram of the estuarine
361 processes affecting phytoplankton biomass distribution in a small-scale, micro-tidal bay. The distribution
362 of these nutrients is further influenced by the surface currents induced by the different winds in the area.
363 With weak down-bay winds (i.e. sea-breeze), stratification is maintained within the estuary, so higher
364 phytoplankton biomass near the discharge points and at the surface layer are found. During strong up-bay
365 and down-bay winds (i.e. North-westerlies, and South-easterlies, respectively), the stratification is broken,
366 so the nutrients discharged from the channels are distributed homogeneously throughout the water column,
367 facilitating phytoplankton growth in the deeper layers. This growth expands horizontally according to the
368 wind-driven currents: towards the inner zone through the lateral shoals, in the case of up-bay winds, or
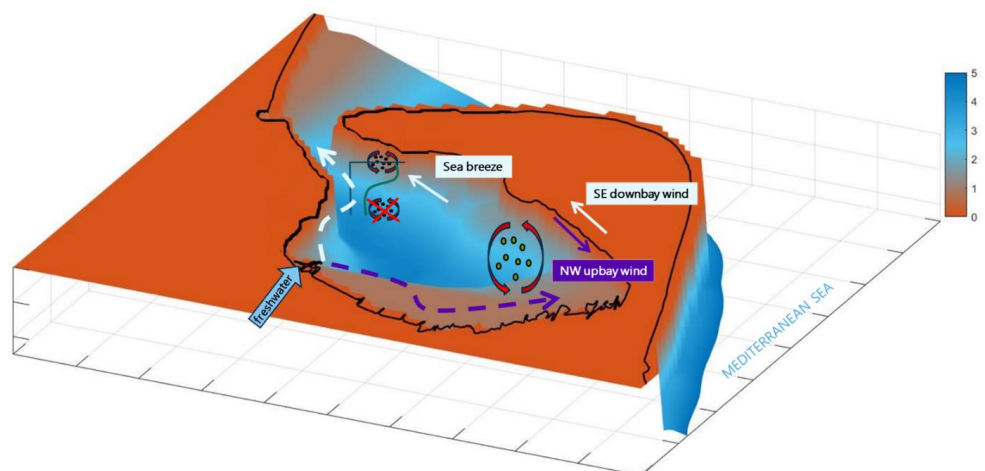369 towards the mouth zone, in the case of down-bay winds.
370

Figure 6. Conceptual diagram of estuarine processes affecting phytoplankton distribution in Fangar Bay. Strong NW up-bay winds cause mixing of the water column and the freshwater plume to move inland. Strong SE down-bay winds also cause mixing, but the freshwater plume moves seaward. Sea breezes also cause a seaward displacement of the freshwater plume, but does not break the vertical stratification, so there is a difference between phytoplankton biomass at the surface and at the bottom.

371
372   Fangar Bay is complex from both a hydrodynamic and biological standpoint. Different phytoplankton
373 patterns are identified depending on the meteorological conditions and, to account for this, different

374   idealised simulations were designed in order to approach each scenario separately. Even so, there are
375   processes that remain unexplored such as the resuspension of Chl *a* containing biomass or the effect of
376   long-duration wind episodes, as well as the change in limiting nutrients that often occurs in such
377   environments, affecting phytoplankton biomass, composition and seasonal cycling (D'Elia et al., 1986;
378   Fisher et al., 1992). The availability of N or P inside the bay also influences the biochemical composition
379   of phytoplankton (Estrada et al., 2008). These topics remain to be studied in future work, as does the
380   analysis of the impact of these dynamics on zooplankton and detritus, which are two variables also taken
381   into account by the ROMS-NPZD model. In any case, the combined analysis of observations and numerical
382   models has provided compelling results and opens new perspectives to understand the short term dynamics
383   of shallow and micro-tidal bays to meteorological events from a combined hydro-biological point of view.

384
385   **6. Appendix A.** Model validation.
386
387   The numerical implementation in Fangar Bay consists of a telescopic three-grid two-way nested ROMS
388   scheme, with a finer bay grid (resolution of about 23 m) embedded within a cascade of coarser grids (see
389   Figure A1). The model has been validated by comparing modelled surface velocities from the coastal
390   domain (~ 350 m) with HFR (High Frequency Radar) data, and modelled currents from the finest domain
391   (~ 23 m) with vertical current profiles measured inside Fangar Bay during an October-November, 2017
392   field campaign. The observational data were, amongst others, current velocity and direction obtained every
393   10 min in 25 cm thick layers distributed from the bottom to the surface.
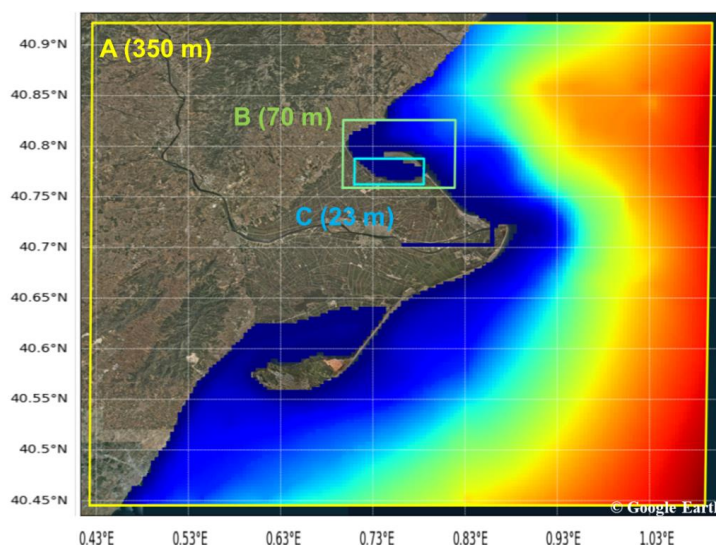394

Figure A1. Ebro Delta and the Fangar Bay, with the telescoping domains used in the system. Conditions for ROMS at the A domain are obtained either from CMEMS-IBI or CMEMS-MED. Map from Google Earth (Data SIO, NOAA, U. S. Navy, NGA, GEBCO, Image Landsat/Copernicus © 2018 Google.
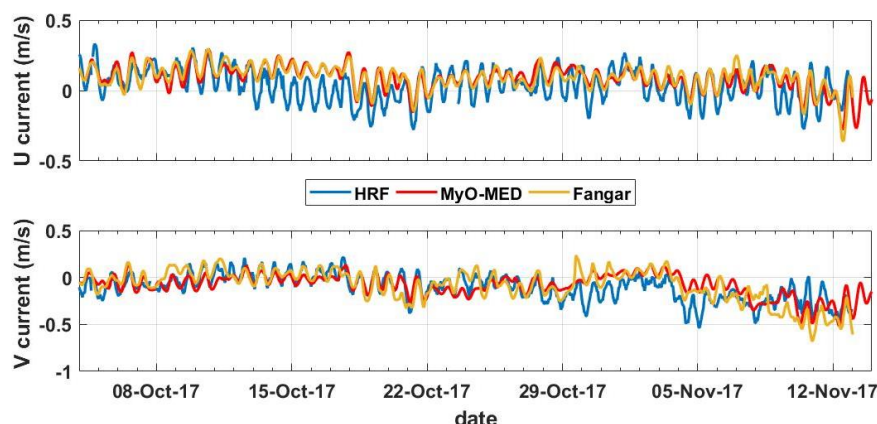
Figure A2. Surface current components U (east-west) and V (north-south) measured by the HRF radar (blue line) and modelled my CMEMS-MED (red) and the Fangar nested suite (yellow) off the Ebro Delta for domain A (350 m).

395

396   The initial and boundary conditions for the coastal domains were obtained from two different CMEMS
397   products (IBI and MED). For the hydrodynamic module, hourly barotropic currents and sea levels are
398   consistently accommodated to the open boundaries with Chapman and Flather algorithms, whereas the
399   variability of currents along the water column (baroclinic component), temperature and salinity are imposed
400   from the CMEMS-IBI daily average values (or hourly data from CMEMS-MED) with clamped conditions.
401   The initial state of the smaller domains is obtained by interpolation from the larger domain conditions.

402

403   The comparison between the HFR and modelled eastward and northward components of the surface
404   currents (Figure A2) revealed good agreement and correlation between both datasets, both in intensity and
405   phase, and for both spatial components. The daily oscillations correspond to the inertial period in the region
406   (~19h) and are well reproduced by the model. Some intensifications of the currents -probably related with
407   energetic wind events- are also well described by the model. For comparison, Figure A2 also plots the
408   current components predicted by CMEMS-MED. For this particular period, the correlation between
409   measured and modelled data shows an $r^2 = 0.63$, slightly larger than the correlation between CMEMS-MED
410   data and measured values.

411

412   Regarding the currents within the bay, the fit between the modelled and measured values is shown in
413   Figure A3. Here, the general trend of the water flow is well captured by the model, which adequately
414   reproduces the main events, in spite of the very low energy of the system. This is a characteristic of both
415   Ebro Delta bays, Fangar and Alfacs (Cerralbo et al., 2014, 2019) although in Fangar it is enhanced by the
416   bay's shallowness and narrow connection with the open sea. For these verification numerical exercises, the
417   6-hourly ECMWF data has been used for the atmospheric forcing. For the hydro-biological simulations
418   shown in this contribution, the 70 m grid has been used because encompasses both the bay and part of the
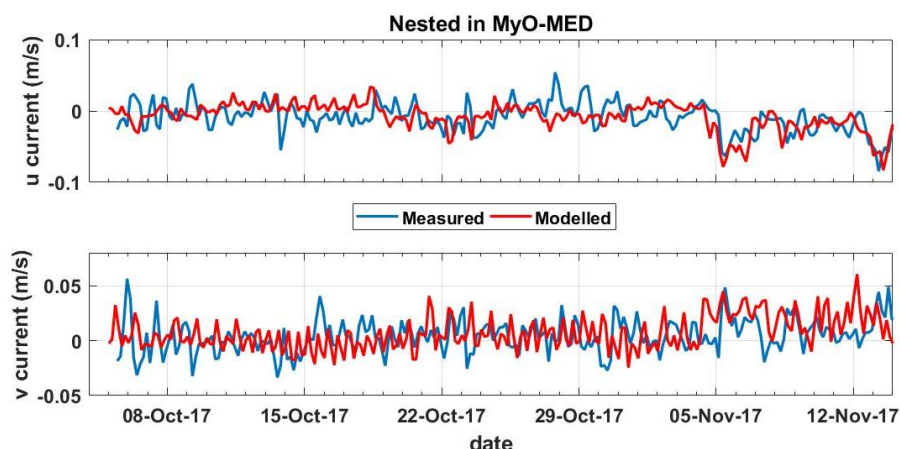419   outer area.

Figure A3. Surface current components U (east-west) and V (north-south) measured inside the bay (blue) and modelled by the Fangar Bay nested scheme (red) during the 2017 autumn field campaign for domain C (23 m). Correspond to boundary forcing provided by CMEMS-MED.

420
421
422 **7. Appendix B.** NPZD Model embedded in ROMS model.
423

424   The NPZD model follows a simple nitrogen-based scheme in order to simulate the interactions of the
425   four variables: nutrients (N), phytoplankton (P), zooplankton (Z) and detritus (D) (Figure B1). The
426   mathematical formulation of the internal fluxes varies in kind and complexity (see review Heinle & Slawig,
427   2013). This annex presents the equations used by the ROMS-NPZD model, as well as the values used for
428   the different parameters, based on Llebot et al. (2010), in the numerical simulations (Table B1).
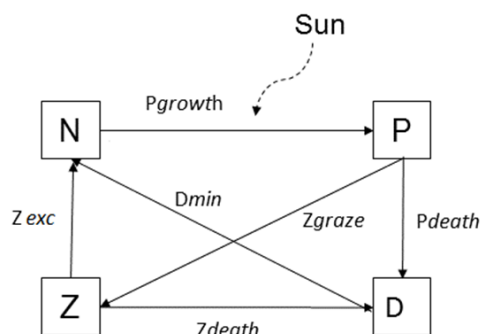

429

430   **Figure B1. ROMS-NPZD model scheme including the transfer functions of the different components. N**
431   **(nutrients), P (phytoplankton), Z (zooplankton) and D (detritus); Pdeath and Zdeath is phytoplankton and**
432   **zooplankton mortality respectively; Pgrowth is phytoplankton growth; Zexc is zooplankton exudation; Zgraze**
433   **is zooplankton grazing and Dmin is remineralization.**

434   <u>**Nutrients**</u>

$$\frac{\partial N}{\partial t} + \mathbf{u} \cdot \nabla N = \delta D + \gamma_n GZ - UP + \frac{\partial}{\partial z}\left(k_v \frac{\partial N}{\partial z}\right), \qquad \text{(B1)}$$

435
436   U = photosynthetic growth and uptake of nitrogen by phytoplankton
437   P = phototrophic phytoplankton
438   Z = herbivorous zooplankton

439   G = grazing on phytoplankton by zooplankton
440   γ_n = some proportion of the consumed phytoplankton being lost directly to the nitrate pool as a function of
441   ''sloppy feeding'' and metabolic processes.
442
443   **Phytoplankton**

$$\frac{\partial P}{\partial t} + \mathbf{u} \cdot \nabla P = UP - GZ - \sigma_d P + \frac{\partial}{\partial z}\left(k_v \frac{\partial P}{\partial z}\right), \quad \text{(B2)}$$

444
445   U = photosynthetic growth and uptake of nitrogen by phytoplankton
446   P = phototrophic phytoplankton
447   Z = herbivorous zooplankton
448   G = grazing on phytoplankton by zooplankton
449   σ_d = phytoplankton mortality
450
451   **Zooplankton**

$$\frac{\partial Z}{\partial t} + \mathbf{u} \cdot \nabla Z = (1 - \gamma_n)GZ - \zeta_d Z + \frac{\partial}{\partial z}\left(k_v \frac{\partial Z}{\partial z}\right), \quad \text{(B3)}$$

452
453   Z = herbivorous zooplankton
454   G = grazing on phytoplankton by zooplankton
455   ζ_d = zooplankton mortality
456   γ_n = some proportion of the consumed phytoplankton being lost directly to the nitrate pool as a function of
457   ''sloppy feeding'' and metabolic processes.
458
459   **Detritus**

$$\frac{\partial D}{\partial t} + \mathbf{u} \cdot \nabla D = \sigma_d P + \zeta_d Z - \delta D + w_d \frac{\partial D}{\partial z} + \frac{\partial}{\partial z}\left(k_v \frac{\partial D}{\partial z}\right), \quad \text{(B4)}$$

460

Grazing $$G = R_m\left(1 - e^{-\Lambda P}\right), \quad \text{(B5)}$$

Uptake $$U = \frac{V_m N}{k_N + N}\frac{\alpha I}{\sqrt{V_m^2 + \alpha^2 I^2}}. \quad \text{(B6)}$$

Irradiance $$I = I_0 \exp\left(k_z z + k_p \int_0^z P(z')dz'\right), \quad \text{(B7)}$$

K_z = light extinction coefficient
k_p = self-shading coefficient

461

462

463 **Table B1. Parameters.**

Parameter name	Symbol	Value	Dimension
Light extinction coefficient	k_z	0.067	m^{-1}
Self-shading coefficient	k_p	0.08	$m^2/$ mmol-N
Initial slope of P-I curve	α	0.025	m^2 W $^{-1}$
Surface irradiance	I_o	158.075	W m^{-2}
Nitrate uptake rate	V_m	1.5	d^{-1}
Phytoplankton mortality rate (senescence)	σ_d	0.15	d^{-1}
Uptake half saturation	k_N	0.8	mmol-N $\cdot$ m^{-3}
Zooplankton excretion efficiency	γ_n	0.03	-
Zooplankton mortality rate	ζ_d	0.08	d^{-1}
Ivlev constant	Λ	0.06	m^3 mmol·N^{-1}
Zooplankton grazing rate	R_m	1.0	d^{-1}
Detritus remineralization rate	δ	0.1	d^{-1}
Detrital sinking rate	w_d	5.0	md^{-1}

464

475
476 **9. Author Contributions:** Conceptualization, methodology, M.F-P.B., M.G., M.E., M.M. and M.F-T.;
477 software, M.F-P.B., M.G., M.F-T., M.M. and M.E.; validation, M.F-P.B., M.M., M.G., M.E. and M.F-T.;
478 formal analysis, M.F-P.B.; investigation, M.F-P.B., M.G., M.E., M.M. and M.F-T.; resources, M.G., M.E,
479 M.M. and M.F-T.; data curation, M.F-P.B., M.M. and M.F.-T.; writing—original draft preparation, M.F-
480 P.B.; writing—review and editing, M.G., M.E., M.M., M.F.-T. and A.S-A; visualization, M.G.;
481 supervision, M.G. and M.E.; project administration, M.E., M.G., M.F-T. and A.S.-A; funding acquisition,
482 M.E., M.F-T and A.S-A. All authors have read and agreed to the published version of the manuscript.

483

484 **10. Conflicts of Interest:** The authors declare no conflict of interest. The funders had no role in the design
485 of the study; in the collection, analyses, or interpretation of data; in the writing of the manuscript, or in the
486 decision to publish the results.
487
488 **11. References**

489 ACA (2012) State of water bodies in Catalonia http://aca-web.gencat.cat/WDMA

490 Ahel, M., Barlow, R. G., and Mantoura, R. F. C. "Effect of Salinity Gradients on the Distribution of
491   Phytoplankton Pigments in a Stratified Estuary." *Mar. Ecol.-Prog. Ser.* 143: 289–295.
492   https://doi.org/https://doi.org/10.3354/meps143289, 1996.

493 Alekseenko, E., B. Roux, A. Sukhinov, R. Kotarba, and D. Fougere. "Nonlinear Hydrodynamics in a
494   Mediterranean Lagoon." *Nonlinear Processes in Geophysics* 20 (2): 189–98.
495   https://doi.org/10.5194/npg-20-189-2013, 2013.

496 Archetti, Genni, Sara Bernia, and Montserrat Salvà-Catarineu. "Análisis de Los Vectores Ambientales Que
497   Afectan La Calidad Del Medio En La Bahía Del Fangar (Delta Del Ebro) Mediante Herramientas
498   SIG." *Revista Internacional de Ciencia y Tecnologia de La Información Geográfica* 10 (1578–5157):
499   252–79, 2010.

500 Artigas, M. L., C. Llebot, O. N. Ross, N. Z. Neszi, V. Rodellas, J. Garcia-Orellana, P. Masqué, J. Piera, M.
501   Estrada, and E. Berdalet. "Understanding the Spatio-Temporal Variability of Phytoplankton Biomass
502   Distribution in a Microtidal Mediterranean Estuary." *Deep-Sea Research Part II: Topical Studies in
503   Oceanography* 101: 180–92. https://doi.org/10.1016/j.dsr2.2014.01.006, 2014.

504 "Automatic Water Quality Information System, DEL EBRO, CHE-Hydrographic Confederation, Quality
505   Alert Network, SAICA Project. Available Online: Https://Www.Saica.Co.Za/ (Accessed on 30
506   January 2020)." 2013.

507 Bolaños, R, G Jorda, J Cateura, J Lopez, J Puigdefabregas, J Gomez, and M Espino. "The XIOM: 20 Years
508   of a Regional Coastal Observatory in the Spanish Catalan Coast." *Journal of Marine Systems* 77 (3):
509   237–60. https://doi.org/10.1016/j.jmarsys.2007.12.018, 2009.

510 Brockmann, Carsten, Roland Doerffer, Marco Peters, Kerstin Stelzer, Sabine Embacher, and Ana Ruescas.
511   "*Evolution of the C2rcc Neural Network for Sentinel 2 and 3 for the Retrieval of Ocean Colour
512   Products in Normal and Extreme Optically Complex Waters*." Living Planet Symposium, 740, 54,
513   2016.

514 Camp, Jordi, and M. Delgado. "*Hidrogafia de Las Bahías Del Delta Del Ebro.*" Inv.Pesq. 51 (3): 351–69,
515   1987.

516 Cerralbo, P., Grifoll, M., Moré, J., Sairouní Afif, A., Espino, M. and Bravo, M.. *"Wind Variability in a
517   Coastal Area (Alfacs Bay, Ebro River Delta)."* Advances in Science and Research 12 (1): 11–21.
518   https://doi.org/10.5194/asr-12-11-2015, 2015.

519 Cerralbo, P., Grifoll, M. and Espino, M. "*Hydrodynamic Response in a Microtidal and Shallow Bay under
520   Energetic Wind and Seiche Episodes."* Journal of Marine Systems 149 (Septembre): 1–13.
521   https://doi.org/10.1016/j.jmarsys.2015.04.003, 2015.

522 Cerralbo, P., Grifoll, M., Valle-Levinson, A. and Espino, M.. "*Tidal Transformation and Resonance in a
523   Short, Microtidal Mediterranean Estuary (Alfacs Bay in Ebre Delta)."* Estuarine, Coastal and Shelf
524   Science 145: 57–68. https://doi.org/10.1016/j.ecss.2014.04.020, 2014.

525 Cerralbo, P., F-Pedrera Balsells, M., Grifoll, M., Fernandez, M., Espino, M., Mestres, M. and Sanchez-
526   Arcilla, A.. "*Use of a Hydrodynamic Model for the Management of the Water Renovation in a Coastal
527   System."* Ocean Science Discussions, 1–20. https://doi.org/10.5194/os-2018-105, 2019

528 D'Elia, C.F., Sanders, J.G., Boynton, W.R. "*Nutrient Enrichment Studies in a Coastal Plain Estuary:
529   Phytoplankton Growth in Large-Scale Continuous Cultures."* Can. J. Fish. Aquat. Sci. 43: 397–406.
530   1986.

531 Delgado, M, and Camp, J. *"Abundancia y Distribución de Nutrientes Inorgánicos Disueltos En Las Bahías
532   Del Delta Del Ero."* Inv.Pesq. 51 (3): 427–41. 1987.

533 Estrada, M., Sala, M.M., van Lenning, K., Alcaraz, M., Felipe, J., Veldhuis, M.J.W. *"Biological*
534   *Interactions in Enclosed Plankton Communities Including Alexandrium Catenella and Copepods:*
535   *Role of Phosphorus."* J. Exp. Mar. Biol. Ecol. 355: 1–11. 2008.

536 F-Pedrera Balsells, M., Grifoll, M., Espino, M., Cerralbo, P. and Sánchez-Arcilla, A. *"Wind-Driven*
537   *Hydrodynamics in the Shallow, Micro-Tidal Estuary at the Fangar Bay (Ebro Delta, NW*
538   *Mediterranean Sea)."* Applied Sciences 10 (19): 6952. https://doi.org/10.3390/app10196952. 2020a.

539 F-Pedrera Balsells, M., Mestres, M., Fernández-Tejedor, M., Cerralbo, P., Espino, M., Grifoll, M. and
540   Sánchez-Arcilla, A. *"Assessing Nature Based Solutions for Managing Coastal Bays."* Journal of
541   Coastal Research 95 (sp1): 1083–87. https://doi.org/10.2112/SI95-211.1. 2020b.

542 F-Pedrera Balsells, M., Grifoll, M., Fernández-Tejedor, M. andl Espino, M. *"Short-Term Response of*
543   *Chlorophyll a Concentration Due to Intense Wind and Freshwater Peak Episodes in Estuaries: The*
544   *Case of Fangar Bay (Ebro Delta)."* Water 13 (5): 701. https://doi.org/10.3390/w13050701. 2021.

545 Fisher, T.R., Peele, E.R., Ammerman, J.W., Harding, L.W. *"Nutrient Limitation of Phytoplankton in*
546   *Chesapeake Bay."* Mar. Ecol. Prog. Ser. 82: 51–63. 1992.

547 Franks, Peter J.S. *"NPZ Models of Plankton Dynamics: Their Construction, Coupling to Physics, and*
548   *Application."* Journal of Oceanography 58 (2): 379–87. https://doi.org/10.1023/A:1015874028196.
549   2002.

550 Garcia, M A, and Ballester, A. *"Notas Acerca de La Meteorología y La Circulación Local En La Región*
551   *Del Delta Del Ebro."* Inv.Pesq., 469–93. 1984.

552 Geyer, N L., Huettel, M. and S. Wetz., M. *"Phytoplankton Spatial Variability in the River-Dominated*
553   *Estuary, Apalachicola Bay, Florida."* Estuaries and Coasts 41 (7): 2024–38.
554   https://doi.org/10.1007/s12237-018-0402-y. 2018.

555 Geyer, W R. *"Influence of Wind on Dynamics and Flushing of Shallow Estuaries."* Estuarine, Coastal and
556   Shelf Science 44 (6): 713–22. https://doi.org/10.1006/ecss.1996.0140. 1997.

557 Gomez, F. A., Lee, S.-K., Liu, Y., Hernandez Jr., F. J., Muller-, and J. T. Karger, F. E., and Lamkin.
558   *"Seasonal Patterns in Phytoplankton Biomass across the Northern and Deep Gulf of Mexico: A*
559   *Numerical Model Study."* Biogeosciences 15: 3561–3576. https://doi.org/https://doi.org/10.5194/bg-
560   15-3561-2018. 2018.

561 Grifoll, M., Navarro, J., Pallares, E., Ràfols, L., Espino, M. and Palomares, A. *"Ocean-Atmosphere-Wave*
562   *Characterisation of a Wind Jet (Ebro Shelf, Nw Mediterranean Sea)."* Nonlinear Processes in
563   Geophysics 23 (3): 143–58. https://doi.org/10.5194/npg-23-143-2016. 2016.

564 Haidvogel, D B, H Arango, W P Budgell, B D Cornuelle, E Curchitser, A F Shchepetkin, C R Sherwood,
565   R P Signell, J C Warner, and J Wilkin. *"Ocean Forecasting in Terrain-Following Coordinates :*
566   *Formulation and Skill Assessment of the Regional Ocean Modeling System."* Journal of
567   Computational Physics, 1–30. https://doi.org/10.1016/j.jcp.2007.06.016. 2007.

568 Heinle, A., and T. Slawig. *"Internal Dynamics of NPZD Type Ecosystem Models."* Ecological Modelling
569   254: 33–42. https://doi.org/10.1016/j.ecolmodel.2013.01.012. 2013.

570 Hickey, B. M. and Banas, N. S. *"Oceanography of the U.S. Pacific Northwest Coastal Ocean and Estuaries*
571   *with Application to Coastal Ecology."* Estuaries 26: 1010–1031.
572   https://doi.org/https://doi.org/10.1007/BF02803360. 2003.

573 Horsburgh, K. J., Hill, A. E., Brown, J., Fernand, L., Garvine, R. W. and Angelico, M. M.P.. *"Seasonal*
574   *Evolution of the Cold Pool Gyre in the Western Irish Sea."* Progress in Oceanography 46 (1): 1–58.
575   https://doi.org/10.1016/S0079-6611(99)00054-3. 2000.

576 Jiang, L., Gerkema, T., Kromkamp, J. C., Van Der Wal, D., Carrasco De La Cruz, P. M. and Soetaert, K..
577   *"Drivers of the Spatial Phytoplankton Gradient in Estuarine-Coastal Systems: Generic Implications*
578   *of a Case Study in a Dutch Tidal Bay."* Biogeosciences 17 (16): 4135–52. https://doi.org/10.5194/bg-
579   17-4135-2020. 2020.

580 Jou, S., Folch, A., Garcia-Orellana, J., Carreño, F. *"Using Freely Available Satellite Thermal Infrared Data*
581   *from Landsat 8 to Identify Groundwater Discharge in Coastal Areas."* Geophysical Research

582   Abstracts 21: p1-1. 1p. 2019.

583   Llebot, C. *"Interactions between Physical Forcing, Water Circulation and Phytoplankton Dynamics in a*
584   *Microtidal Estuary."* PhD Thesis. http://digital.csic.es/handle/10261/100958?locale=es. 2010.

585   Llebot, C., Rueda, F. J., Solé, J., Lara Artigas, M. and Estrada, M. *"Hydrodynamic States in a Wind-Driven*
586   *Microtidal Estuary (Alfacs Bay)."* Journal of Sea Research 85 (3–4): 263–76.
587   https://doi.org/10.1016/j.seares.2013.05.010. 2014.

588   Llebot, C., Solé, J., Delgado, M., Fernández-Tejedor, M., Camp, J. and Estrada, M. *"Hydrographical*
589   *Forcing and Phytoplankton Variability in Two Semi-Enclosed Estuarine Bays."* Journal of Marine
590   Systems 86 (3–4): 69–86. https://doi.org/10.1016/j.jmarsys.2011.01.004. 2011.

591   Llebot, C., Spitz, Y. H., Solé, J. and Estrada, M. *"The Role of Inorganic Nutrients and Dissolved Organic*
592   *Phosphorus in the Phytoplankton Dynamics of a Mediterranean Bay: A Modeling Study."* Journal of
593   Marine Systems 83 (3–4): 192–209. https://doi.org/10.1016/j.jmarsys.2010.06.009. 2010.

594   Lohrenz SE, Fahnenstiel GL, Redalje DG, Lang GA, Chen X, Dagg MJ. *"Variations in Primary Production*
595   *of Northern Gulf of Mexico Continental Shelf Waters Linked to Nutrient Inputs from the Mississippi*
596   *River."* Marine Ecology Progress Series 155: 45–54. https://www.int-
597   res.com/abstracts/meps/v155/p45-54/.1997.

598   Martin, M. A., Fram, J. P., and Stacey, M. T. *"Seasonal Chlorophyll a Fluxes between the Coastal Pacific*
599   *Ocean and San Francisco Bay."* Mar. Ecol.-Prog. Ser. 337: 51–61.
600   https://doi.org/https://doi.org/10.3354/meps337051. 2007.

601   Muñoz, I. *"Limnología de La Part Baixa Del Riu Ebre i Els Canals de Reg: Els Factors Fisico-Quimics,*
602   *El Fitoplancton i Els Macroinvertebrats Bentonics".* PhD thesis, Facultad de Biología. Universidad
603   de Barcelona. 1990.

604   Perez, M., Camp, J. *"Distribución Espacial y Biomasa de Las Fanerógamas Marinas de Las Bahías Del*
605   *Delta Del Ebro".* 50: 519–30. 1986.

606   Powell, T. M, Craig V W Lewis, N Curchitser, E., Haidvogel, D. B., Hermann, A. J. and Dobbins, E. L.
607   *"Results from a Three-Dimensional, Nested Biological-Physical Model of the California Current*
608   *System and Comparisons with Statistics from Satellite Imagery."* Journal of Geophysical Research:
609   Oceans 111 (7): 1–14. https://doi.org/10.1029/2004JC002506. 2006.

610   Ramón, M, Fernández, M. and Galimany, E. "*Development of Mussel (Mytilus Galloprovincialis) Seed*
611   *from Two Different Origins in a Semi-Enclosed Mediterranean Bay (N.E. Spain).*" Aquaculture 264
612   (1–4): 148–59. https://doi.org/10.1016/j.aquaculture.2006.11.014. 2007.

613   Reguera, B., Bravo, I., Mariño, J., Campos, M.J., Fraga, S., Carbonell, A. "*Trends in the Occurrence of*
614   *Dinophysis Spp. in Galician Coastal Waters."* Toxic Phytoplankton Blooms in the Sea. Elsevier,
615   559–564. 1993.

616   Rico, J. E. Cruz. *"Análisis de La Variabilidad de La Clorofila En La Bahía de Todos Santos a Través de*
617   *Un Modelo Numérico Físico-Biológico."* PhD Thesis. Centro de Investigación Científica y de
618   Educación Superior de Ensenada, Baja California. 2015.

619   Shchepetkin, A. F., and McWilliams, J. C. *"The Regional Oceanic Modeling System (ROMS): A Split-*
620   *Explicit, Free-Surface, Topography-Following-Coordinate Oceanic Model."* Ocean Modelling 9 (4):
621   347–404. https://doi.org/10.1016/j.ocemod.2004.08.002. 2005.

622   Simpson, J. H., and D. Bowers. *"Models of Stratification and Frontal Movement in Shelf Seas."* Deep Sea
623   Research Part A. Oceanographic Research Papers 28 (7): 727–38. https://doi.org/10.1016/0198-
624   0149(81)90132-1. 1981.

625   Soetaert, K., Middelburg, J. J., Heip, C., Meire, P., Van Damme, and T. S., and Maris. *"Long-Term Change*
626   *in Dissolved Inorganic Nutrients in the Heterotrophic Scheldt Estuary (Belgium, The Netherlands)."*
627   Limnol. Oceanogr. 51: 409–423. https://doi.org/https://doi.org/10.4319/lo.2006.51.1_part_2.0409.
628   2006.

629   Soriano-González, J., Angelats, E., Fernández-Tejedor, M., Diogene, J. and Alcaraz, C. *"First Results of*
630   *Phytoplankton Spatial Dynamics in Two NW-Mediterranean Bays from Chlorophyll-A Estimates*

631   *Using Sentinel 2: Potential Implications for Aquaculture."* Remote Sensing 11 (15).
632   https://doi.org/10.3390/rs11151756. 2019.

633 Srichandan, S., Kim, J. Y., Kumar, A., Mishra, D. R., Bhadury, and G. P., Muduli, P. R., Pattnaik, A. K.,
634   and Rastogi. *"Interannual and Cyclone-Driven Variability in Phytoplankton Communities of a
635   Tropical Coastal Lagoon."* Mar. Pollut. Bull. 101: 39–52.
636   https://doi.org/https://doi.org/10.1016/j.marpolbul.2015.11.030. 2015.

637 Stow, C. A., Jolliff, J., McGillicuddy Jr., D. J., Doney, S. C., Allen, J. I., Friedrichs, M. A., and P. M., Rose,
638   K. A., y Walhead. *"Skill Assessment for Coupled Biological/Physical Models of Marine Systems."*
639   Journal of Marine Systems 76: 4–15. 2009.

640 Wan, Y., Chelsea Qiu, Doering, P., Ashton, M. Detong Sun, and Coley, T. *"Modeling Residence Time with
641   a Three-Dimensional Hydrodynamic Model: Linkage with Chlorophyll a in a Subtropical Estuary."*
642   Ecological Modelling 268: 93–102. https://doi.org/10.1016/j.ecolmodel.2013.08.008. 2013.

643 Warner, J. C., Geyer, W. R., and Lerczak, J A. *"Numerical Modeling of an Estuary: A Comprehensive Skill
644   Assessment."* Journal of Geophysical Research: Oceans 110 (C05001).
645   https://doi.org/10.1029/2004JC002691. 2005.

646 Xie, Xiaohui, and Ming Li. *"Effects of Wind Straining on Estuarine Stratification: A Combined
647   Observational and Modeling Study."* Journal of Geophysical Research: Oceans 123 (4): 2363–80.
648   https://doi.org/10.1002/2017JC013470. 2018.

649